

ON THE FORMATION OF OZONE IN SOLAR SYSTEM OXYGEN ICES EXPOSED TO HEAVY IONS

COURTNEY ENNIS¹ AND RALF I. KAISER^{1,2}

¹ Department of Chemistry, University of Hawaii at Manoa, Honolulu, HI 96822, USA; ralfk@hawaii.edu

² UH NASA Astrobiology Institute, University of Hawaii at Manoa, Honolulu, HI 96822, USA

Received 2011 May 20; accepted 2011 September 8; published 2012 January 5

ABSTRACT

Mimicking the bombardment of icy surfaces with heavy ions from solar system radiation fields, solid-phase molecular oxygen ($^{32}\text{O}_2$) and its isotope labeled analogue ($^{36}\text{O}_2$) were irradiated with monoenergetic carbon (C^+), nitrogen (N^+), and oxygen (O^+) ions in laboratory experiments simulating the interaction of ions from the solar wind and those abundant in planetary magnetospheres. Online Fourier-transform infrared spectroscopy of the irradiated oxygen ices (12 K) showed that the yields of molecular ozone monomer ($\text{O}_3 \sim 2 \times 10^{-3}$ molecules eV^{-1} in $^{32}\text{O}_2$) were independent of the mass of the implanted C^+ , N^+ , and O^+ ions ($\Phi_{\text{max}} = 4.0 \times 10^{14}$ ions cm^{-2}). The production of oxygen atoms in the solid was observed in the mid-IR stabilized via the $[\text{O}_3 \dots \text{O}]$ van der Waals complex. We expand on this inference by comparing the ozone yields induced by light particles (e^- , H^+ , and He^+) to the heavy ions (C^+ , N^+ , and O^+) to provide compelling evidence that the abundance of radiolytic products in an oxygen-bearing solid is primarily dependent on electronic stopping regimes, which supersedes the contribution of nuclear stopping processes irrespective of the mass of the particle irradiation in the kinetic energy regime of solar wind and magnetospheric particles.

Key words: astroparticle physics – infrared: general – molecular processes – planets and satellites: surfaces – radiation mechanisms: general

Online-only material: color figures

1. INTRODUCTION

Ubiquitous within the confines of the solar system and beyond in the interstellar medium (ISM), ionizing radiation fields contain a wide distribution of particles from electrons to heavy nuclei with varying kinetic energies (E_k —from eV magnitudes to relativistic regimes up to a few PeV). Galactic cosmic rays (GCRs) comprise mainly protons (p , H^+) and helium nuclei (α -particles, He^{2+}) with a smaller component of heavier nuclei such as C, N, and O ions that possess E_k peaking at ~ 0.1 GeV nucleon $^{-1}$ (Gloeckler 1979; Johnson 1990). Within the solar system environment, the solar wind is an additional source of energetic particles (H^+ , He^{2+} , and heavy ions: $E_k \sim 1$ keV amu^{-1} at 1 AU) playing an important role in the surface processing of airless bodies. Furthermore, charged species are observed in the planetary magnetospheres of, for instance, Jupiter (C, O, and S ions; Anglin et al. 1997; Radioti et al. 2005) and Saturn (N and O ions; Cooper et al. 2001; Young et al. 2005; Sittler et al. 2006, 2008). These species possess energies ranging from only a few eV (e.g., suprathermal pick-up ions generated in an orbiting body ionosphere) to over 100 MeV heavy ions. Magnetospheric species are often sourced internally from carbon, nitrogen, and oxygen-bearing molecules, such as methane (CH_4 ; Atreya et al. 2006; Bennett et al. 2006), ammonia (NH_3 ; Smith et al. 2008), and water (H_2O ; Zheng et al. 2009), which are often observed within planetary atmospheres and surfaces.

Due to the compounded effect of these radiation sources within the solar system, a planetary body is continually exposed to energetic particles (Kaiser & Roessler 1998; Hudson & Moore 2001). The airless and icy moons of Jupiter and Saturn form a planetary context for the present study, where heavy ion processing is expected to take place. In addition, GCR heavy ions irradiate the surfaces of outer solar system bodies such as Triton, Trans-Neptunian objects (TNOs—such as Pluto, Charon), Kuiper Belt Objects (KBOs), and comets (Moore et al.

2004). The chemical alteration of a surface by the transfer of energy from a heavy ion via elastic nuclear stopping (S_n) and inelastic electronic stopping (S_e) interactions is the primary focus for this experimental study. S_n interactions lead to, for example, ‘knock-on’ particles produced by homolytic bond cleavage of a target molecule; within the classical billiard model, this is induced by the direct collision with an impinging ion within the atoms of the solid. Alternately, S_e interactions lead to ionization and unimolecular decomposition of a target molecule and the release of a secondary electron (ionization) and suprathermal atoms and radical fragments (unimolecular decomposition) to the matrix. These secondary electrons are born with kinetic energies of up to a few keV allowing them to ionize target molecules successively, producing a cascade of electrons in the ice. Both stopping regimes act to generate a significant density of atoms and ions in a low-temperature planetary surface (30–100 K), the reaction mechanisms of which will be theoretically and experimentally examined.

Here, these effects will be simulated by selecting solid molecular oxygen (O_2) as the target condensate in the present experiments. Online Fourier-transform infrared spectroscopy (FTIR) will be used to monitor the formation of ozone (O_3) induced by the irradiation of monoenergetic (5 keV) carbon (C^+), nitrogen (N^+), and oxygen (O^+) ions. As molecular oxygen does not absorb in the mid-infrared (mid-IR) region, the spectrum of oxygen target does not interfere with the detection of ozone or the signatures of any of molecular products that could be formed via the implantation of the impinging ion (e.g., carbon monoxide (CO) or carbon dioxide (CO_2) for C^+ irradiation). Although selected to be representative of an ice surface in terms of the chemical processing induced by energetic particle irradiation, condensed-phase oxygen has been detected on the Jovian moons Europa, Callisto (Spencer & Calvin 2002), and Ganymede (Spencer et al. 1995) via its 577 nm visible absorption band (Calvin & Spencer 1997), which is active for

Table 1
Irradiation Parameters

Particle	Target	Current (nA)	Implants ($\times 10^{14}$ ions)	Total Energy ($\times 10^{18}$ eV)	Dose (eV O ₂ molecule ⁻¹)
C ⁺	³² O ₂	2.5 ± 1.0	2.3 ± 0.9	1.12 ± 0.45	29.3 ± 16.9
	³⁶ O ₂	7.0 ± 1.0	6.3 ± 0.4	3.15 ± 0.23	81.5 ± 20.0
N ⁺	³² O ₂	12.5 ± 2.0	11.2 ± 2.2	5.62 ± 1.12	172.0 ± 64.5
	³⁶ O ₂	15.0 ± 2.0	13.5 ± 1.8	6.74 ± 0.90	204.0 ± 63.0
O ⁺	³² O ₂	6.0 ± 2.0	4.0 ± 1.3	2.02 ± 0.67	69.0 ± 35.0
	³⁶ O ₂	10.0 ± 1.0	9.0 ± 0.9	4.49 ± 0.45	151.3 ± 41.6

an interacting pair of oxygen molecules. In addition, molecular oxygen can be inferred to exist by the presence of its radiolytic product ozone (O₃; Kasting & Catling 2003) which has been identified on the surfaces of Ganymede (Noll et al. 1996), Rhea, and Dione (Noll et al. 1997). Observed to be stable at surface temperatures (90–150 K) above the species sublimation temperature, molecular oxygen is most likely accumulated in pores, defects, and ion tracks of irradiated water ice (Johnson & Jessor 1997) from which it is formed (Spencer & Calvin 2002; Zheng et al. 2006a, 2006b). However, detailed quantitative measurement of the temporal ozone column densities generated by heavy ion interaction with the solid molecular oxygen, combined with subsequent analysis of the ozone formation pathway, is expected to clarify the understanding of heavy particle irradiation pertaining to oxygen-bearing astrophysical surfaces.

2. EXPERIMENTAL

The experiments were performed in a stainless steel chamber that was evacuated to ultrahigh vacuum (UHV) conditions ($1.0 \pm 0.2 \times 10^{-10}$ torr). Within the chamber, a highly polished 31.75×31.75 mm silver substrate was attached to the cold head of a closed-cycle helium refrigerator (CTI-Cryogenics CP-1020), which cooled the substrate to a temperature of 12.0 ± 0.5 K—measured by a Lakeshore DT-470 silicon diode sensor. Here, pure ice samples were created by depositing oxygen (³²O₂—BOC Gases: Grade 5.0) or isotope labeled oxygen (³⁶O₂—Cambridge Isotope Laboratories Inc: 97%) gas onto the cooled substrate. An oxygen gas base pressure of 2.0×10^{-8} torr was used for deposition over a 10 minute condensation period and was monitored for contaminants using a Balzer QMG 420 quadrupole mass spectrometer (QMS—operating in residual gas analyzer mode with electron impact energy of 100 eV at a 0.3 mA emission current). Gas-phase molecular abundances measured by the QMS over the sublimation period of the oxygen condensates indicated that the samples were of 140 ± 30 nm thickness (confer details on this procedure in Ennis et al. 2011). An ion source (SPECS IQE 12/38) supplied with a 2.0×10^{-4} torr base pressure of high-purity carbon dioxide (CO₂: BOC Gases: Grade 5.0), nitrogen (N₂: Airgas: Grade 5.0), or oxygen (O₂: BOC Gases: Grade 5.0) gas was used to produce the charged particles. Positioned after the ionization and extraction regions of the ion source, a Wien mass filter separated unwanted ions to produce a monoenergetic beam of 5 keV C⁺, N⁺, or O⁺ ions directed at the substrate (Ennis et al. 2011). A target mounted Faraday cup was used to measure the ion currents (Table 1) scanned over a target area of 0.50 ± 0.06 cm². The ice samples were then irradiated for 4 hr isothermally at 12.0 ± 0.5 K where online analysis of the solid state was performed by FTIR spectroscopy (Nicolet 6700). Here, the 6000–500 cm⁻¹ mid-IR spectra were compiled from

196 individual scans collected over 2.0 minutes at a resolution of 2 cm⁻¹. Ion trajectories through the oxygen target were simulated using the Stopping and Range of Ions in Matter (SRIM) Monte Carlo program (Ziegler et al. 2008). These calculations showed that the maximum stopping range for the impinging ions (Table 2) was always less than the 140 ± 30 nm sample thickness; implying that the complete transfer of C⁺, N⁺, and O⁺ ion kinetic energy (5 keV) to the sample was achieved for the respective experiments. Subsequently, the average *dose* (eV molecule⁻¹) absorbed by an individual oxygen molecule in the samples could be calculated (Table 1). Following the irradiation procedure, the solid molecular oxygen samples were then heated to 300 K (at a rate of 0.5 K minute⁻¹) using the temperature control unit (Lakeshore 331). This enabled the identification of the volatile oxygen molecules, together with any radiolytic products formed during irradiation, at their respective sublimation temperatures using the online QMS.

3. RESULTS

3.1. Qualitative Analysis

The mid-IR spectra collected for the pristine molecular oxygen ice (blank), and after the irradiation of C⁺, N⁺, and O⁺ ions, at 12.0 ± 0.5 K are shown in Figure 1. Here, we observe that the pure molecular oxygen does not show any absorption signature for the perturbed species in the solid state (~ 1550 cm⁻¹; Freiman & Jodl 2004) as previously identified in thicker oxygen samples ($1.7 \pm 0.7 \times 10^3$ nm; Ennis et al. 2011). Following irradiation of the oxygen samples with C⁺, N⁺, and O⁺ ions, the most prominent absorption bands observed in the mid-IR spectra were assigned to molecular ozone (O₃) displaying a C_{2v} bent structure. For molecular ozone (⁴⁸O₃) derived from neat molecular oxygen (³²O₂), the absorption bands for the ν_3 asymmetric stretching fundamental and the $\nu_1 + \nu_3$ combination band were located at 1040 cm⁻¹ and 2105 cm⁻¹, respectively, adhering to assignments previously made for solid ozone in the literature (Brewer & Wang 1972). For ozone (⁵⁴O₃) formed from the isotope-substituted oxygen (³⁶O₂), the absorption band for the ν_3 (⁵⁴O₃) asymmetric stretching mode was identified at its 980 cm⁻¹ redshifted position. However, the $\nu_1 + \nu_3$ (⁵⁴O₃) combination band could not be observed above the signal-to-noise threshold at its expected 1990 cm⁻¹ position (Brewer & Wang 1972). Upon closer inspection of the fine structure of the highest intensity ν_3 asymmetric stretching absorption band of ozone (Figure 2), the peak is a superposition of three separate moieties. The separation of the absorption peak into its individual components follows the analysis performed by Bennett & Kaiser (2005) that investigated the temporal evolution ($t = 1$ hr) of ozone generated from an analogous molecular oxygen ice via 5 keV electron irradiation (Bennett & Kaiser 2005). The most significant contribution to the peak

Table 2
Theoretical Ion Stopping Characteristics

Particle	Range (nm)	Electronic LET(S_e) (keV μm^{-1})	Nuclear LET(S_n) (keV μm^{-1})	Vacancies ^a (ion ⁻¹)	[O ₃] _{max} ^b ($\times 10^{17}$ molecules cm^{-2})
³² O ₂ ice: 1.54 g cm^{-3}					
C ⁺	26.4	35.1	109.9	251 (180)	4.02 (2.88)
N ⁺	22.5	37.8	140.4	257 (184)	4.11 (2.94)
O ⁺	20.2	35.8	171.1	265 (189)	4.24 (3.02)
³⁶ O ₂ ice: 1.72 g cm^{-3}					
C ⁺	26.5	35.1	102.0	251 (180)	4.02 (2.88)
N ⁺	22.7	37.8	131.0	257 (184)	4.11 (2.94)
O ⁺	20.4	35.7	160.6	265 (190)	4.24 (3.04)

Notes.

^a Oxygen atom displacement energy of 5.2 eV (7.1 eV).

^b Theoretical maximum ozone abundance after $\Phi = 4.0 \times 10^{14}$ ions cm^{-2} .

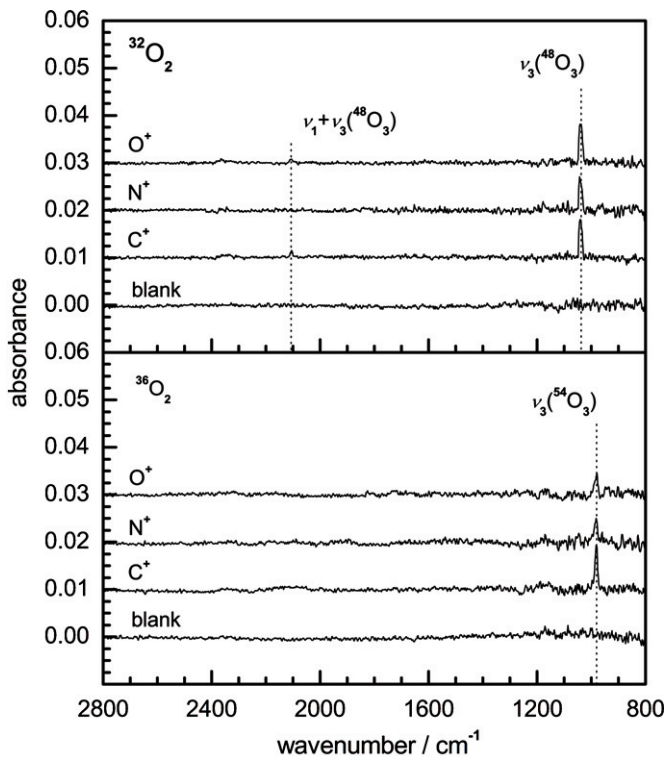


Figure 1. Mid-IR spectra of molecular oxygen surfaces (12 K), before (blank) and after exposure to C⁺, N⁺, and O⁺ ions.

intensity originates from the ν_3 fundamental of the isolated ozone monomer centered at 1038 cm^{-1} . The formation of an interacting pair (dimer) of ozone molecules in the oxygen matrix $[\text{O}_3 \dots \text{O}_3]$ yields an absorption peak at a slightly blueshifted position of 1044 cm^{-1} . Finally, the van der Waals complex formed between molecular ozone and atomic oxygen $[\text{O}_3 \dots \text{O}]$ in the solid matrix results in the appearance of an absorption band located at 1033 cm^{-1} . This species is not clearly resolved in the spectra collected at the completion of ion irradiation, but is evident in the spectra collected during the first minutes of irradiation. The collated spectra for each system were resolved individually using a Gaussian fitting program where integrated peak areas were calculated for each of the three overlapping bands.

The qualitative detection of solid state molecular species by FTIR spectroscopy can be correlated to the gas-phase analysis

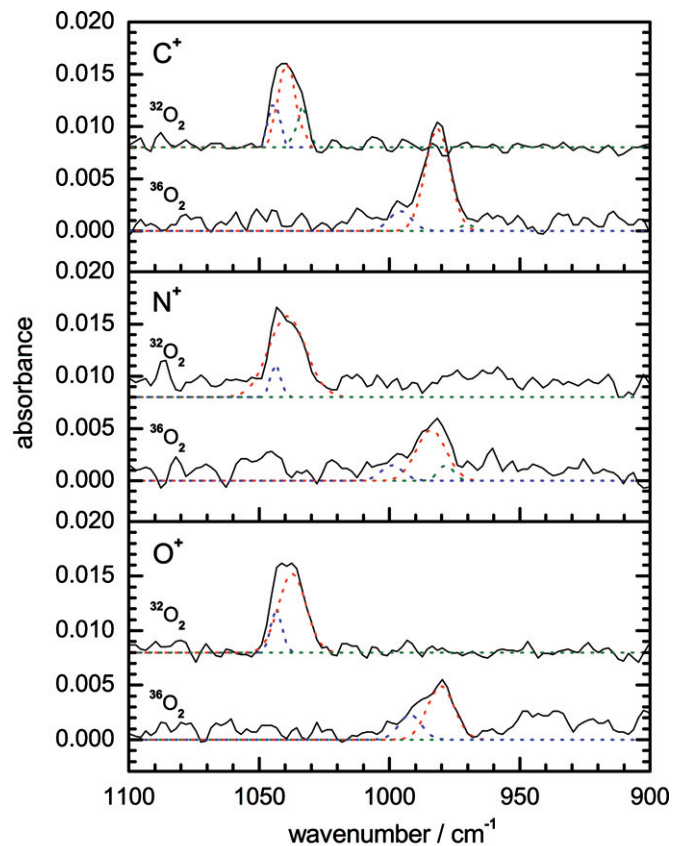


Figure 2. Gaussian fits for ozone monomer (O₃, red), ozone dimer ([O₃...O₃], blue), and the ozone-atomic oxygen complex ([O₃...O], green) superimposed over the $\nu_3(\text{O}_3)$ mid-IR absorption band for all irradiated ice spectra.

(A color version of this figure is available in the online journal.)

of the sublimating condensates using mass spectrometry. After controlled heating of the substrate to a temperature of 25 K, the oxygen ice starts to sublime (Figure 3). Here, we observe an increase in mass-to-charge signal for singularly ionized molecular oxygen (O_2^+ ; $m/z = 32$) and its isotope labeled analogue ($m/z = 36$) detected by the QMS instrument after electron impact within the residual gas analyzer. For each experiment, the molecular oxygen ion current is observed to peak at $\sim 1 \times 10^{-7}$ A at 32 K, with the sublimation profiles closely following those obtained for the non-irradiated (blank) experiments (Figure 3, dotted format). The irradiated samples

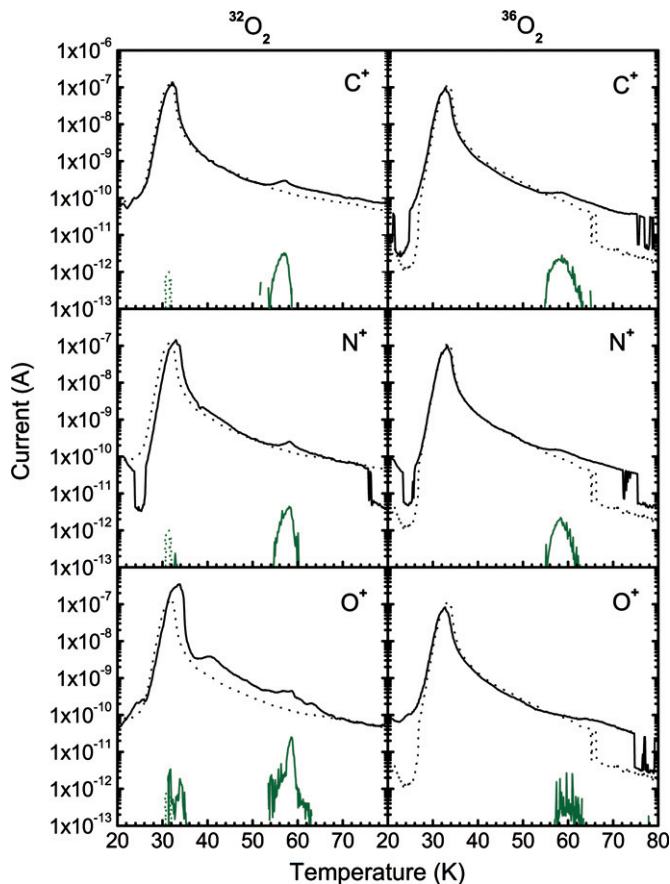


Figure 3. Ion current (A) of molecular oxygen ($m/z = 32$ or 36 , black) and ozone ($m/z = 48$ or 54 , green) as a function of substrate temperature (K), as recorded during the sublimation of the molecular oxygen condensates by QMS. (A color version of this figure is available in the online journal.)

all display an increase in the ozone gas-phase abundance (O_3^+ ; $m/z = 48$ and 54) to a peak ion current of $\sim 5 \times 10^{-11}$ A. With no signal pertaining to ozone identified in the blank samples, the sublimation of ozone from the irradiated samples occurs at a substrate temperature between 55 and 65 K. Note that the increase in $m/z = 48$ signal observed during the sublimation (30–35 K) of the oxygen $^{32}O_2$ condensate for the O^+ irradiation experiment is likely due to ion–molecule reactions within the residual gas analyzer of the QMS and not due to molecular ozone $^{48}O_3$ (~ 55 K). Although some ozone could thermally desorb from the surface with the rapidly sublimating oxygen component, we expect the cross section to be much smaller than the amount of ozone formed in the residual gas analyzer at this temperature (Bennett & Kaiser 2005; Ennis et al. 2011). Mass-to-charge signals for irradiation products such as carbon monoxide (CO^+ ; $m/z = 28$) and carbon dioxide (CO_2^+ ; $m/z = 44$); molecular nitrogen (N_2^+ ; $m/z = 28$), nitric oxide (NO^+ ; $m/z = 30$), nitrous oxide (N_2O^+ ; $m/z = 44$), and nitrogen dioxide (NO_2^+ ; $m/z = 46$) for the C^+ and N^+ irradiation of oxygen ($^{32}O_2$), respectively (mass-to-charge signals altered for the $^{36}O_2$ samples), were programmed for QMS detection. However, none of these species were observed to increase in gas-phase abundance above the 1×10^{-13} A QMS detection limit during sample sublimation.

3.2. Quantitative Analysis

Molecular ozone and its van der Waals complex with atomic oxygen have been identified as the sole radiolytic products for

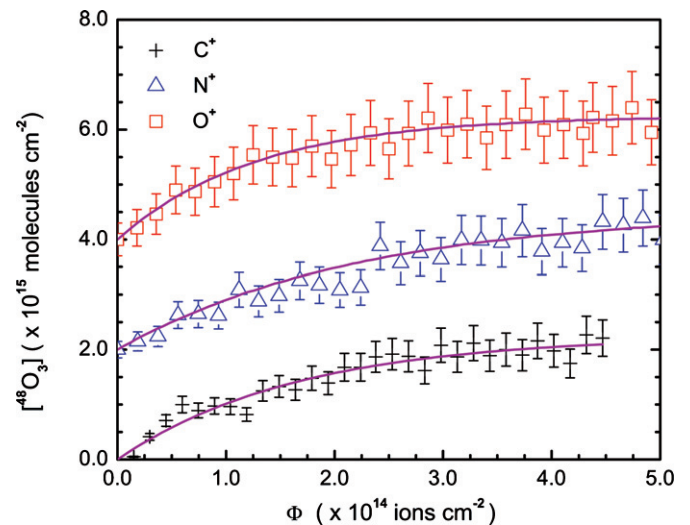


Figure 4. Calculated ozone ($^{48}O_3$) abundances in oxygen ($^{32}O_2$) ice as a function of C^+ (no offset), N^+ (2×10^{15} molecules cm^{-2} offset), and O^+ (4×10^{15} molecules cm^{-2} offset) ion fluence.

(A color version of this figure is available in the online journal.)

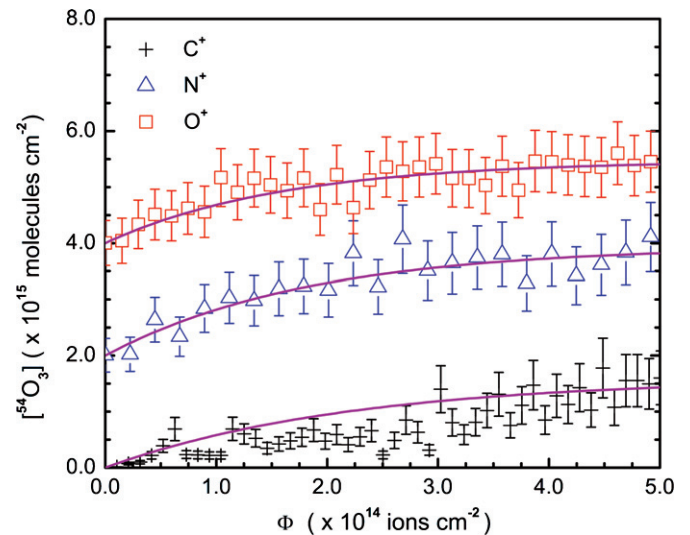


Figure 5. Calculated ozone ($^{54}O_3$) abundances in oxygen ($^{36}O_2$) ice as a function of C^+ (no offset), N^+ (2×10^{15} molecules cm^{-2} offset), and O^+ (4×10^{15} molecules cm^{-2} offset) ion fluence.

(A color version of this figure is available in the online journal.)

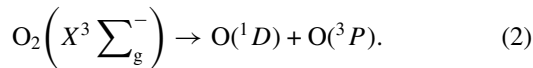
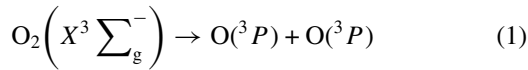
molecular oxygen ice exposed to heavy ion irradiation. It follows that quantitative analysis of the ozone abundances induced by C^+ , N^+ , and O^+ ion irradiation over the exposure period can be performed. For each system, a total C^+ , N^+ , and O^+ fluence of 4.0×10^{14} ions cm^{-2} was sufficient to reach the maximum $^{48}O_3$ (Figure 4) or $^{54}O_3$ (Figure 5) abundance in the solid state, as indicated by the intensity of the ozone ν_3 fundamental absorption band reaching a threshold in the FTIR spectra. Note that the error associated with the calculation of ozone column densities (i.e., error bars for Figures 4 and 5) necessitates manual fitting of kinetic parameters. Although the fitted kinetic profiles to some data sets appear to be increasing at the completion of irradiation (4.0×10^{14} ions cm^{-2}), successive absorption band areas were within $\pm 5\%$ to indicate that the maximum ozone column density had been reached. The integrated ozone ν_3 absorption bands were then converted to column densities (molecules cm^{-2}) using a modified Lambert–Beer

expression (Bennett et al. 2004). An experimentally derived (Adler-Golden et al. 1985) integrated absorption coefficient (A -value) of 1.53×10^{-17} cm molecule $^{-1}$ was used for the $\nu_3(^{48}\text{O}_3)$ calculations. A relative A -value of 1.72×10^{-17} cm molecule $^{-1}$ for the $\nu_3(^{54}\text{O}_3)$ asymmetric stretching vibration was then calculated from theoretical work on the ozone isotopomer (Sivaraman et al. 2011). The resultant ozone ($^{48}\text{O}_3$) abundances, plotted as a function of C^+ , N^+ , and O^+ ion fluence, are shown in Figure 4 (15% error bars derived from integration of the ozone absorption band intensities are appended to the data points). Maximum ozone ($^{48}\text{O}_3$) column densities are measured to be $2.05 \pm 0.21 \times 10^{15}$ molecules cm $^{-2}$ for C^+ irradiation, $2.09 \pm 0.19 \times 10^{15}$ molecules cm $^{-2}$ for N^+ irradiation, and $2.15 \pm 0.20 \times 10^{15}$ molecules cm $^{-2}$ for O^+ irradiation. Similarly for $^{54}\text{O}_3$, Figure 5 displays the fluence-dependent column densities where maximum ozone ($^{54}\text{O}_3$) abundances are observed to be $1.35 \pm 0.15 \times 10^{15}$ molecules cm $^{-2}$ for C^+ irradiation, $1.73 \pm 0.22 \times 10^{15}$ molecules cm $^{-2}$ for N^+ irradiation, and $1.34 \pm 0.47 \times 10^{15}$ molecules cm $^{-2}$ for O^+ irradiation.

4 DISCUSSION

4.1. Molecular Oxygen Destruction

Irradiation of the condensates by energetic C^+ , N^+ , and O^+ ions results in the homolytic cleavage of the molecular oxygen precursor resulting in a pair of oxygen atoms. It has previously been determined via electron impact experiments (Cosby 1993) that the radiolytic dissociation of oxygen follows two major reaction pathways. The first pathway (formally spin-forbidden) has a barrier of 5.16 eV (Reaction (1)), while the second (spin-allowed) has an entrance barrier of 7.13 eV (Reaction (2)):



Note that for dissociation to proceed, the oxygen molecule must be excited to a repulsive potential energy surface ~ 6 eV (Reaction (1)) or ~ 8 eV (Reaction (2)) above the ground state. Also note that half of the oxygen atoms produced from Reaction (2) are in the first electronically excited state $\text{O}(^1D)$; however in the solid state, the lifetime of an excited oxygen atom is of the order of a few hundred milliseconds before the species undergoes relaxation to the ground state $\text{O}(^3P)$ (Mohammed 1990). The nascent oxygen atoms generated by these two pathways are borne with excess kinetic energies of up to a few eV, which may be sufficient to overcome any diffusion barrier associated with its matrix position, liberating the atom to engage in non-equilibrium processes.

Energy to promote the excitation and dissociation of the oxygen molecules is transferred by the impinging C^+ , N^+ , and O^+ ions via nuclear stopping (S_n) and electronic stopping (S_e) processes in the solid. First, for S_n interactions, the transmitted particle can elastically collide with a target oxygen molecule resulting in the direct ejection of an oxygen atom (i.e., “knock-on” atom) from its initial position following the dissociation of the molecular oxygen covalent bond. In fact, a heavy ion with initial kinetic energy of 5 keV can undergo multiple interactions as it slows in the solid and its translational energy is dissipated. These events produce numerous “vacancies” (i.e., interstitial cavity where oxygen molecules once resided before collision) and hence a collision cascade; with each vacancy inferring the

production of two oxygen atoms from direct nuclear interaction. The number of vacancies generated for a specific ion can be calculated using SRIM Monte Carlo simulations (Ziegler et al. 2008) and are compiled for 5 keV C^+ , N^+ , and O^+ ions in Table 2. After averaging the trajectories and interactions of 10,000 individual ions implanted within a molecular oxygen target ($^{32}\text{O}_2$: $\rho = 1.54$ g cm $^{-3}$, $^{36}\text{O}_2$: $\rho = 1.73$ g cm $^{-3}$), and for the displacement energies of 5.16 eV and 7.13 eV associated with each oxygen dissociation channel, note that each ion is calculated to generate hundreds vacancies before coming to rest (range in nm). In addition, the SRIM calculations provide the linear energy transfer (LET; in keV μm^{-1}) values for the 5 keV C^+ , N^+ , and O^+ ions transferred to the solid via S_n (Table 2). Here, we observe that $\text{LET}(S_n)$ is correlated to the mass of the impinging particle, with C^+ ions transferring 109.9 keV μm^{-1} as they come to rest in the oxygen ($^{32}\text{O}_2$) ice, compared to the more massive O^+ ions with an $\text{LET}(S_n)$ of 171.1 keV μm^{-1} .

Alternately, S_e interactions, induced by inelastic interaction with the impinging particle and a solid target, result in the ionization and/or unimolecular decomposition via homolytic bond rupture of the oxygen molecules, generating “secondary” electrons that possess kinetic energies of up to a few keV. These secondary electrons can efficiently ionize additional target molecules they encounter—in effect generating a cascade of electrons. Although a total number of secondary electrons generated per impinging ion is not calculable, previous experiments (Ennis et al. 2011) comparing electron and light particle (H^+ and He^+) irradiation of molecular ices (O_2 and CO_2) provided evidence that S_e processes exerted a higher influence on the radiolytic product yield over S_n processes. The SRIM calculations have also provided the electronic stopping LET component for the 5 keV C^+ , N^+ , and O^+ ions in solid oxygen (Table 2). Here, we observe that the $\text{LET}(S_e)$ does not show any dependence on the mass of the particle within the error limits, with C^+ , N^+ , and O^+ ions all transferring 35–38 keV μm^{-1} as they come to rest in both the oxygen $^{32}\text{O}_2$ or $^{36}\text{O}_2$ solids.

4.2. Ozone Formation

As observed in the infrared spectra for oxygen ice irradiated with fast electrons (Bennett & Kaiser 2005), the detection of both the $[\text{O}_3 \dots \text{O}]$ complex and the isolated O_3 monomer in the present ion irradiation experiments implies separate non-equilibrium processes involving atomic oxygen propagate in the low-temperature matrix. If considering a pair of adjacent oxygen molecules $(\text{O}_2)_2$ in the matrix, the irradiation-induced dissociation of a single oxygen molecule can theoretically form an $[\text{O}_2 \dots \text{O} \dots \text{O}]$ complex. One of the suprathreshold oxygen atoms of the complex can then react with the oxygen molecule to form the observed $[\text{O}_3 \dots \text{O}]$ complex. If the remaining oxygen atom has insufficient energy to escape, the complex will be preserved in the low-temperature ices. Alternatively, as the suprathreshold oxygen atoms are borne with excess kinetic energy (up to 2 eV), a significant number are expected to have sufficient energy to overcome the diffusion barrier of the matrix. This allows for these oxygen atoms to react without barrier after collision with an oxygen molecule distant from its formation site, resulting in the production of an ozone monomer (Reaction (3)) as primarily observed in the infrared spectra (Figure 2):

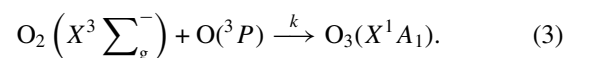


Table 3
Ozone Formation Parameters

$^{32}\text{O}_2 + ^{16}\text{O} \xrightarrow{k} ^{48}\text{O}_3$		
Particle	$[\text{O}_2]_0$ (molecules cm^{-2})	k ($\text{cm}^2 \text{ion}^{-1}$)
C ⁺	$2.25 \pm 0.12 \times 10^{15}$	$6.0 \pm 0.3 \times 10^{-15}$
N ⁺	$2.50 \pm 0.06 \times 10^{15}$	$4.5 \pm 0.3 \times 10^{-15}$
O ⁺	$2.25 \pm 0.06 \times 10^{15}$	$7.8 \pm 0.5 \times 10^{-15}$
$^{36}\text{O}_2 + ^{18}\text{O} \xrightarrow{k} ^{54}\text{O}_3$		
Particle	$[\text{O}_2]_0$ (molecules cm^{-2})	k ($\text{cm}^2 \text{ion}^{-1}$)
C ⁺	$1.47 \pm 0.05 \times 10^{15}$	$6.2 \pm 0.5 \times 10^{-15}$
N ⁺	$1.94 \pm 0.07 \times 10^{15}$	$5.5 \pm 0.5 \times 10^{-15}$
O ⁺	$1.60 \pm 0.14 \times 10^{15}$	$4.5 \pm 1.2 \times 10^{-15}$

If we assume that Reactions (1) and (2) unfold at a faster rate than Reaction (3), the formation of ozone in the ion-irradiated molecular oxygen ice at 12 K should follow the pseudo-first-order growth model. We denote $[\text{O}_3]_\Phi$ as the column density (molecules cm^{-2}) of ozone formed at a specific ion fluence, Φ (ions cm^{-2}), from an initial abundance of molecular oxygen $[\text{O}_2]_0$ in the solid, at a fluence-dependent reaction rate, k ($\text{cm}^2 \text{ion}^{-1}$). Now we fit the formation of ozone to the experimental data using the first-order growth model shown in Equation (4). Please note that $[\text{O}_2]_0$ is the total abundance of molecular oxygen that partakes in Reaction (3), not the total oxygen abundance in the solid, and that $[\text{O}_2]_0 = [\text{O}_3]_\infty$; the maximum column density of ozone observed after ion irradiation is

$$[\text{O}_3]_\Phi = [\text{O}_2]_0 (1 - e^{-k\Phi}). \quad (4)$$

The best fits for Equation (4) are appended to the ozone abundance profiles in Figure 4 for $^{48}\text{O}_3$ and Figure 5 for $^{54}\text{O}_3$, while the optimized parameters for the molecular oxygen precursor abundance, $[\text{O}_2]_0$, and the fluence-dependent reaction rate, k , are compiled in Table 3 for each individual experiment. Here we observe that the C⁺, N⁺, and O⁺ ion-induced formation of ozone, from both the $^{32}\text{O}_2$ or $^{36}\text{O}_2$ molecular oxygen solids, all proceed at a fluence-dependent reaction rate of $\sim 4\text{--}8 \times 10^{-15} \text{ cm}^2 \text{ion}^{-1}$. There is no discernible trend between the calculated reaction rate and the mass of the impinging particle, as was apparent for the ozone abundances from the integrated spectra.

Referring back to the number of vacancies produced per fast ion implant via S_n interactions, we can calculate a maximum ozone abundance resultant from these processes for each system. With each vacancy generating two oxygen atoms, we assume that each oxygen atom then on-reacts with an oxygen molecule to form ozone (i.e., 100% efficiency). The expected maximum column densities for ozone, $[\text{O}_3]_{\text{max}}$, are displayed in Table 2 at a C⁺, N⁺, or O⁺ ion fluence of $\Phi = 4.0 \times 10^{14}$ ions cm^{-2} . Here we observe that $[\text{O}_3]_{\text{max}} \sim 4 \times 10^{17}$ molecules cm^{-2} for an oxygen atom displacement energy of 5.2 eV and $[\text{O}_3]_{\text{max}} \sim 3 \times 10^{17}$ molecules cm^{-2} for an oxygen atom displacement energy of 7.3 eV, associated with Reactions (1) and (2), respectively. Note that these theoretical maximum ozone column densities are two orders of magnitude higher than the experimental ozone abundances measured from the integrated absorption bands in the FTIR spectra, indicating either that a substantial amount of ozone is destroyed by continual heavy ion irradiation and/or that the oxygen atoms react back to molecular oxygen. Likewise, the low temperature matrix can “store” oxygen atoms at 12 K.

Table 4
Comparative Ozone Formation Yields

Particle	Penetration Depth (nm)	Dose ^c (eV molecule ⁻¹)	O ₃ yield ^d (molecules eV ⁻¹)	LET(S_e) (keV μm^{-1})
e^- ^a	330.0	2.1 ± 0.6	$2.6 \pm 1.8 \times 10^{-3}$	15.2
H ⁺ ^b	137.0	5.1 ± 2.3	$4.1 \pm 1.8 \times 10^{-3}$	27.4
He ⁺ ^b	77.0	9.0 ± 3.3	$1.7 \pm 0.6 \times 10^{-3}$	28.3
C ⁺	26.4	26.2 ± 16.4	$2.0 \pm 1.2 \times 10^{-3}$	35.1
N ⁺	22.5	30.8 ± 13.1	$2.1 \pm 0.8 \times 10^{-3}$	37.8
O ⁺	20.2	34.3 ± 19.1	$2.1 \pm 1.1 \times 10^{-3}$	35.8

Notes.

^a Bennett & Kaiser (2005)—electron irradiation area $3.0 \pm 0.4 \text{ cm}^2$.

^b Ennis et al. (2011).

^c Dose per $^{32}\text{O}_2$ molecule to a particle fluence of $\Phi = 4.0 \times 10^{14}$ particles cm^{-2} .

^d O₃ yield via $^{32}\text{O}_2$ irradiation to a particle fluence of $\Phi = 4.0 \times 10^{14}$ particles cm^{-2} .

4.3 Comparison between Heavy Ion Irradiation and Electrons and Light Ion Irradiation

Due to the reaction rates calculated above for ozone formation in irradiated molecular oxygen ices being normalized to the fluence of C⁺, N⁺, and O⁺ ions impinging the target (k in $\text{cm}^2 \text{ion}^{-1}$), we cannot directly compare these results to the kinetic reaction rates (k in s^{-1}) previously determined for ozone formation induced by electron (Bennett & Kaiser 2005) and light ion (H⁺ and He⁺; Ennis et al. 2011) irradiation. However, as all particle irradiation sources (Table 4) were performed with monoenergetic 5 keV beams, we can compare the calculated molecular ozone yields (molecules eV⁻¹) as generated by a normalized particle fluence of 4.0×10^{14} ions cm^{-2} . Note that as the experimental beam currents of the particles range from a constant 100 nA for the electrons, to a low 19 ± 4 nA for H⁺, and a considerably higher 290 ± 52 nA for He⁺, as well as the beam currents obtained for the present C⁺, N⁺, and O⁺ ion beams (Table 1), the irradiation time (s) taken to reach the arbitrary 4.0×10^{14} ions cm^{-2} fluence differs considerably.

As these monoenergetic particles impinge a solid oxygen surface, there is an inverse correlation between the calculated penetration depth and the mass of the particles, ranging from 330.0 nm for electrons to only 20.2 nm for O⁺ ions. It follows that we can determine the total number of oxygen molecules in the irradiation volume (product of the penetration depth and irradiation surface area: $0.50 \pm 0.06 \text{ cm}^2$ for ions and $3.0 \pm 0.4 \text{ cm}^2$ for electrons). The average energy supplied to each oxygen molecule (*dose*, in eV molecule⁻¹) after 4.0×10^{14} particles cm^{-2} ($E_k = 5 \text{ keV}$) are slowed and ultimately implanted in the target can be subsequently calculated; obtaining a direct correlation between the *dose* and the mass of the incident particle (Table 4). However, we observe no correlation between the *dose* transmitted to the molecular oxygen precursor and the yield of product ozone molecules as a particle fluence of 4.0×10^{14} particles cm^{-2} is reached for the different systems. If the radiolytic processing of molecular oxygen ice to form ozone was primarily driven by S_n interactions, we would expect a general correlation between these two parameters as the number density of “knock-on” oxygen atoms is dependent on the mass of the impinging particle. As this is evidently not the case, we can then assume that S_e interactions play the more significant role of the two stopping regimes in terms of ozone formation. This can be justified when comparing the LET(S_e) (in keV μm^{-1}) obtained from SRIM code for the various particle

sources (Table 4; note that the 5 keV electrons transfer their kinetic energy exclusively via electronic stopping processes). It is calculated that all particles possess $\text{LET}(S_e)$ values within the same order of magnitude (i.e., 15–40 keV μm^{-1} —independent of particle mass) that would result in the similar experimental ozone yields displayed in Table 4 ($\sim 1.5\text{--}4 \times 10^{-3}$ molecules eV^{-1}). The inference that electronic stopping interactions are the dominant processes pertaining to ozone formation in oxygen ice exposed to energetic particle irradiation supports our previous experimental studies involving H^+ and He^+ ions (Ennis et al. 2011).

5. ASTROPHYSICAL AND PLANETARY IMPLICATIONS

This experimental study has used infrared spectroscopy to qualitatively identify ozone as the primary molecular product generated in solid molecular oxygen via the implantation of fast C^+ , N^+ , and O^+ ions. In addition, ozone was detected in the gas phase during the sublimation of the oxygen condensates by mass spectrometry. Online measurement of the solid-state ozone abundances during its formation showed that the yield of ozone displayed no dependence on the mass of the irradiating particle. This finding infers that the radiolytic processing of oxygen ice is primarily driven by electronic stopping interactions (S_e) between the impinging ion and the target, compared to nuclear stopping interactions (S_n) which would show a strong correlation between the product yield and the mass of the particle. As both secondary electrons and “knock-on” oxygen atoms can induce the formation of the ozone product, the results imply that the number density of secondary electrons in the solid, generated by target molecule ionization through electronic stopping interactions, is significantly larger than the number of “knock-on” oxygen atoms produced by direct collisions between the C^+ , N^+ , and O^+ ions and the target oxygen molecules (i.e., nuclear stopping interactions). The prevalence for electronic stopping interactions to dictate the yield of molecular product in a solid exposed with energetic particles has been previously observed with oxygen-containing molecular ices (carbon monoxide: Bennett et al. 2009, 2010; carbon dioxide: Bennett et al. 2004; Ennis et al. 2011; molecular oxygen: Bennett & Kaiser 2005; Ennis et al. 2011) irradiated with light particles (e^- , H^+ , and He^+) in experimental studies previously investigated by the workgroup. However, in accordance with the results of the present study, we suggest this inference can be extended to irradiation with heavier particles such as C^+ , N^+ , and O^+ ions; even though their nuclear stopping interactions are calculated to have significantly higher LET values (Table 2) than their electronic stopping component.

The present study has also determined the formation rate for ozone induced by the exposure of a molecular oxygen ice to C^+ , N^+ , and O^+ ions at 12 K, as a function of ion fluence to a maximum of $\Phi = 4.0 \times 10^{14}$ ions cm^{-2} . Beyond this exposure limit the abundance of ozone molecules in the condensate levels off ($\sim 2.0 \times 10^{15}$ molecules cm^{-2} in $^{32}\text{O}_2$ ice and $\sim 1.5 \times 10^{15}$ molecules cm^{-2} in $^{36}\text{O}_2$ ice) before the ozone formation and destruction processes are presumed to reach equilibrium in the irradiated solid. Placing the irradiation conditions in an astrophysical context, GCR radiation (MeV component) has a very low solar system flux ($\phi = 1\text{--}10$ particles $\text{cm}^{-2} \text{s}^{-1}$; Cooper et al. 1998) of heavy ions including C^+ , N^+ , and O^+ . Therefore, the present experiments simulate $\sim 10^6$ years of processing an airless outer solar system body, such as Triton, Pluto, and KBOs, by these particles. Shorter processing periods (~ 100 years) could be expected for the

satellite surfaces of the Jovian and Saturnian systems due to the higher flux of heavy ions experienced within these planets extended magnetospheres (e.g., 10 keV O^+ ions in the Jovian environment: $\phi \sim 10^4$ particles $\text{cm}^{-2} \text{s}^{-1}$; Radioti et al. 2005). We have calculated that the LET values for the heavy ions undergoing electronic stopping interactions ($\text{LET}(S_e) = 15\text{--}40$ keV μm^{-1}) would result in ozone production yields of $\sim 1.5\text{--}4.0 \times 10^{-3}$ molecules eV^{-1} (or a maximum of ~ 160 ozone molecules μm^{-1}) for a pure molecular oxygen surface exposed to C^+ , N^+ , and O^+ ions. However, as pure oxygen surfaces have not been detected on any astrophysical body, but rather as small clusters of condensed oxygen (Calvin & Spencer 1997; Spencer & Calvin 2002) residing in a water ice matrix after its radiolytic formation (Orlando & Sieger 2003; Johnson et al. 2005; Zheng et al. 2006a, 2006b), these ozone abundances must be scaled down to reflect their trace abundances within these environments. Note that these previous investigations involving the irradiation of water ice with fast particles have shown that nascent oxygen atoms readily react with water molecules to form hydrogen peroxide (H_2O_2), which can then undergo successive dehydrogenation events to form molecular oxygen within the water ice matrix. Here, molecular oxygen can also scavenge atomic oxygen to form ozone; completing one of many alternate reaction pathways that can influence the column density of the species. However, we suggest that such water ice matrices do not directly apply to the present study; yet, they may be the subject of future work.

Although molecular oxygen is not observed to be a dominant component of astrophysical ices within the observable regions of the solar system, we suggest that the underlying principle highlighted in this study—that the yield of molecular products from an irradiated molecular oxygen surface is primarily dependent on electronic stopping interactions—can be extended to involve more universally detected oxygen-bearing ices. Carbon monoxide and carbon dioxide are two such species that have been detected in the solid state in higher abundances relative to molecular oxygen on solar system bodies (Gibb et al. 2004; Cruikshank et al. 2010) and TNOs (Owen et al. 1993). Upon exposure to energetic particle irradiation, these species undergo homolytic bond rupture to produce suprathreshold oxygen atoms, analogous to the radiation-induced destruction molecular oxygen. Reactions involving the nascent oxygen atoms form abundances of molecular oxygen, ozone, and a suite of carbon-oxides (Jamieson et al. 2007a, 2007b, 2007c; Bennett et al. 2010)—all detected in the solid state during experimental simulation of these particle–target interactions. We conclude that electronic stopping interactions would play the more significant role in the observed abundances of these radiolytic products—in comparison to nuclear stopping interactions—induced by the implantation of the particle in the solid and that the observed product yield is independent on the mass of the impinging particle. Furthermore, the results of this study suggest that chemical alteration of the solid should proceed at an increased rate due to the number density of secondary electrons generated by electronic stopping interactions in the matrix. It follows that the abundance of secondary electrons induced by electronic stopping processes generate reactive ions and radicals at rates greatly above that generated by direct nuclear interactions. As we expect this to be the case for an impinging particle irrespective of its mass, we could expect chemical processing to propagate on icy oxygen-bearing surfaces at similar rates; even if these surfaces are exposed to radiation fields with varying distributions of light to heavy particles.

C.E. and R.I.K. thank the W. M. Keck Foundation for support. R.I.K. also acknowledges partial support from the National Aeronautics and Space Administration through the NASA Astrobiology Institute (Cooperative Agreement No. NNA09DA77A issued through the Office of Space Science).

REFERENCES

- Adler-Golden, S. M., Langhoff, S. R., Bauschlicher, C. W., Jr., & Carney, G. D. 1985, *J. Chem. Phys.*, **83**, 255
- Anglin, J. D., Burrows, J. R., Mu, J. L., & Wilson, M. D. 1997, *J. Geophys. Res.*, **102**, 1
- Atreya, S. K., Adams, E. Y., Niemann, H. B., et al. 2006, *Planet. Space Sci.*, **54**, 1177
- Bennett, C. J., Jamieson, C., Mebel, A. M., & Kaiser, R. I. 2004, *Phys. Chem. Chem. Phys.*, **6**, 735
- Bennett, C. J., Jamieson, C. S., & Kaiser, R. I. 2009, *ApJS*, **182**, 1
- Bennett, C. J., Jamieson, C. S., & Kaiser, R. I. 2010, *Phys. Chem. Chem. Phys.*, **12**, 4032
- Bennett, C. J., Jamieson, C. S., Osamura, Y., & Kaiser, R. I. 2006, *ApJ*, **653**, 792
- Bennett, C. J., & Kaiser, R. I. 2005, *ApJ*, **635**, 1362
- Brewer, L., & Wang, J. L.-F. 1972, *J. Chem. Phys.*, **56**, 759
- Calvin, W. M., & Spencer, J. R. 1997, *Icarus*, **130**, 505
- Cooper, J. F., Christian, E. R., & Johnson, R. E. 1998, *Adv. Space Res.*, **21**, 1611
- Cooper, J. F., Johnson, R. E., Mauk, B. H., Garrett, H. B., & Gehrels, N. 2001, *Icarus*, **149**, 133
- Cosby, P. C. 1993, *J. Chem. Phys.*, **98**, 9560
- Cruikshank, D. P., Meyer, A. W., Brown, R. H., et al. 2010, *Icarus*, **206**, 561
- Ennis, C. P., Bennett, C. J., & Kaiser, R. I. 2011, *Phys. Chem. Chem. Phys.*, **13**, 9469
- Freiman, Y. A., & Jodl, H. J. 2004, *Phys. Rep.*, **401**, 1
- Gibb, E. L., Whittet, D. C. B., Boogert, A. C. A., & Tielens, A. G. G. M. 2004, *ApJS*, **151**, 35
- Gloeckler, G. 1979, *Rev. Geophys. Space Phys.*, **17**, 569
- Hudson, R. L., & Moore, M. H. 2001, *J. Geophys. Res.*, **106**, 33275
- Jamieson, C. S., Mebel, A. M., & Kaiser, R. I. 2007a, *Chem. Phys. Lett.*, **440**, 105
- Jamieson, C. S., Mebel, A. M., & Kaiser, R. I. 2007b, *Chem. Phys. Lett.*, **443**, 49
- Jamieson, C. S., Mebel, A. M., & Kaiser, R. I. 2007c, *Chem. Phys. Lett.*, **450**, 312
- Johnson, R. E. 1990, *Energetic Charged-Particle Interactions with Atmospheres and Surfaces* (Berlin: Springer)
- Johnson, R. E., Cooper, P. D., Quickenden, T. I., Grieves, G. A., & Orlando, T. M. 2005, *J. Chem. Phys.*, **123**, 184715
- Johnson, R. E., & Jesser, W. A. 1997, *ApJ*, **480**, 79
- Kaiser, R. I., & Roessler, K. 1998, *ApJ*, **503**, 959
- Kasting, J. F., & Catling, D. 2003, *ARA&A*, **41**, 429
- Mohammed, H. H. 1990, *J. Chem. Phys.*, **93**, 412
- Moore, M. H., Hudson, R. L., & Ferrante, R. F. 2004, *Earth Moon Planets*, **92**, 291
- Noll, K. S., Johnson, R. E., Lane, A. L., Domingue, D. L., & Weaver, H. A. 1996, *Science*, **273**, 341
- Noll, K. S., Roush, T. L., Cruikshank, D. P., Johnson, R. E., & Pendleton, Y. J. 1997, *Nature*, **388**, 45
- Orlando, T. M., & Sieger, M. T. 2003, *Surf. Sci.*, **528**, 1
- Owen, T. C., Roush, T. L., Cruikshank, D. P., et al. 1993, *Science*, **261**, 745
- Radioti, A., Krupp, N., Woch, J., et al. 2005, *J. Geophys. Res.*, **110**, 1
- Sittler, E. C., Andre, N., Blanc, M., et al. 2008, *Planet. Space Sci.*, **56**, 3
- Sittler, E. C., Jr., Johnson, R. E., Smith, H. T., et al. 2006, *J. Geophys. Res.*, **111**, A09223
- Sivaraman, B., Mebel, A. M., Mason, N. J., Babikov, D., & Kaiser, R. I. 2011, *Phys. Chem. Chem. Phys.*, **13**, 421
- Smith, H. T., Shappirio, M., Johnson, R. E., et al. 2008, *J. Geophys. Res.*, **113**, A11206
- Spencer, J. R., & Calvin, W. M. 2002, *AJ*, **124**, 3400
- Spencer, J. R., Calvin, W. M., & Person, M. J. 1995, *J. Geophys. Res.*, **100**, 19049
- Young, D. T., Berthelier, J.-J., Blanc, M., et al. 2005, *Science*, **307**, 1262
- Zheng, W., Jewitt, D., & Kaiser, R. I. 2006a, *ApJ*, **639**, 534
- Zheng, W., Jewitt, D., & Kaiser, R. I. 2006b, *ApJ*, **648**, 753
- Zheng, W., Jewitt, D., & Kaiser, R. I. 2009, *J. Phys. Chem. A*, **113**, 11174
- Ziegler, J. F., Ziegler, M. D., & Biersack, J. P. 2008, *The Stopping Range of Ions in Solids* (New York: Pergamon)